

Effect of thermally induced structural disorder on the chemical durability of International Simple Glass

Frédéric Angeli, Thibault Charpentier, Patrick Jollivet, Dominique de Ligny, Michael Bergler, Alexander Veber, S. Gin, Hong Li

▶ **To cite this version:**

Frédéric Angeli, Thibault Charpentier, Patrick Jollivet, Dominique de Ligny, Michael Bergler, et al.. Effect of thermally induced structural disorder on the chemical durability of International Simple Glass. npj Materials Degradation, 2018, 2 (1), pp.31. 10.1038/s41529-018-0052-3 . cea-01872240

HAL Id: cea-01872240
https://cea.hal.science/cea-01872240

Submitted on 11 Sep 2018

HAL is a multi-disciplinary open access archive for the deposit and dissemination of scientific research documents, whether they are published or not. The documents may come from teaching and research institutions in France or abroad, or from public or private research centers.

L'archive ouverte pluridisciplinaire **HAL**, est destinée au dépôt et à la diffusion de documents scientifiques de niveau recherche, publiés ou non, émanant des établissements d'enseignement et de recherche français ou étrangers, des laboratoires publics ou privés.

npj | Materials Degradation

www.nature.com/npjmatdeg

ARTICLE OPEN

Effect of thermally induced structural disorder on the chemical durability of International Simple Glass

Frederic Angeli[1], Thibault Charpentier[2], Patrick Jollivet[1], Dominique de Ligny[3], Michael Bergler[3], Alexander Veber[3], Stéphane Gin[1] and Hong Li[4]

While the influence of silicate oxide glass composition on its chemical durability is increasingly known, the contribution of structure only is less well understood, yet is crucial for an accurate description of aqueous alteration mechanisms. The effect of structural disorder can be investigated by varying the thermal history of the glass. Furthermore, the structural changes generated by self-irradiation in nuclear glasses can be compared with those induced by fast quenching. In the context of deep geological disposal of vitreous matrices, it is then challenging to address the structural impact on glass durability. Here, a borosilicate glass, the International Simple Glass, was fiberized to obtain a rapidly quenched sample. The quenching rate and fictive temperature were evaluated from in situ Raman and Brillouin spectroscopies. Multinuclear nuclear magnetic resonance was used to obtain insight into the effect of quenching on the pristine and altered glass structure. Higher bond angle distribution and lower mixing of alkalis were observed in the fast quenched glass. Some of AlO_4 groups are then Ca-compensated, while a part of BO_4 is transformed into BO_3 units. The structural modifications increase the hydrolysis of the silicate network occurring in the forward rate regime at 90 °C by a factor of 1.4–1.8 depending on the pH value. Residual rate regime is similarly affected, more significantly at the beginning of the experiments conducted in silica saturated solutions. These findings prove that the reactivity of glass remains controlled by its structure under the various alteration regimes.

npj Materials Degradation (2018)2:31 ; doi:10.1038/s41529-018-0052-3

INTRODUCTION

The physico-chemical properties of silicate oxide glasses depend strongly on the nature and the relative proportions of the cations in their composition. The effects of these different elements on the chemical durability of glasses have been widely studied in various domains ranging from bioglasses with medical applications,[1] materials used to regulate the CO_2 cycle,[2] lead crystal glass found in drinking vessels[3] or vitreous matrices fabricated to confine radioactive waste.[4] Understanding and modeling the behavior of nuclear waste packages in contact with groundwater is essential in the context of a deep geological disposal of vitreous matrices.[5] The resulting glass composition can vary widely depending on the waste composition; in this context the effects of the major elements of nuclear glasses on the various alteration regimes have been investigated in depth (see for example Gin et al.[6] and the references therein). Their exact roles can however be difficult to ascertain since comparing different glasses involves both structural and chemical composition changes that are difficult to separate. To consider only structural changes, the chemical composition has to be kept constant. This can be achieved by modifying only the thermal history of the glass. Variations in the geometric and chemical disorder can then be evaluated as a function of the glass quenching rate.[7]

This approach may be particularly relevant to better understanding the structural damages induced by self-irradiation in nuclear glasses due to alpha decay of minor actinides. The displacement cascades induced by the recoil nuclei generated by alpha decay may induce the same kind of structural reorganizations in borosilicate glasses as do a very rapid thermal quench, leading to a new structural state at a fictive temperature higher than that of the pristine glass.[8–10] When the whole volume is damaged, the accumulation of additional displacements in the glass structure does not modify it significantly anymore. Some properties, such as mechanical properties or density, reach then a plateau.[11] However, glasses submitted to external heavy-ion irradiation, simulating the effect of the recoil nuclei, show more significant effects than those seen in ^{244}Cm doped glasses.[12,13] This behavior was attributed to the local annealing induced by the alpha particle's loss of electronic energy that partially repairs the damages generated by the recoil nuclei.[14] Structural changes induced by self-irradiation could in particular affect the alteration behavior of glass matrices. Rapidly quenched glass may thus constitute a representative sample to investigate the chemical durability of these glasses in a laboratory setting. The hyper-quenched glasses, as fibers, are not however easy to handle and reliable direct measurement of their fictive temperatures by the classical calorimetric method is challenging.[15] To overcome this difficulty, we proposed here to use the Raman and Brillouin spectral signature of the cooling rate. Due to this new approach, an initial calibration of the spectroscopic evolution with the cooling rate was conducted on one bulk sample.

It has been shown that hydrogen diffusivity increases in soda-lime glasses during alteration at pH 1 when the fictive temperature increases.[16] The lower density of these glasses may

[1]CEA, DEN, DE2D, SEVT, LCLT, CEA Marcoule, 30207 Bagnols-sur-Ceze, France; [2]NIMBE, CEA, CNRS, Université Paris-Saclay, CEA Saclay, 91191 Gif-sur-Yvette Cedex, France; [3]Institute of Glass and Ceramics, DMSE, University of Erlangen-Nuremberg, DE 91058 Erlangen, Germany and [4]Nippon Electric Glass, Shelby, Pittsburg, PA 15024, USA
Correspondence: Frederic Angeli (frederic.angeli@cea.fr)

Received: 9 April 2018 Revised: 27 August 2018 Accepted: 27 August 2018
Published online: 11 September 2018

Published in partnership with CSCP and USTB

npj nature partner journals

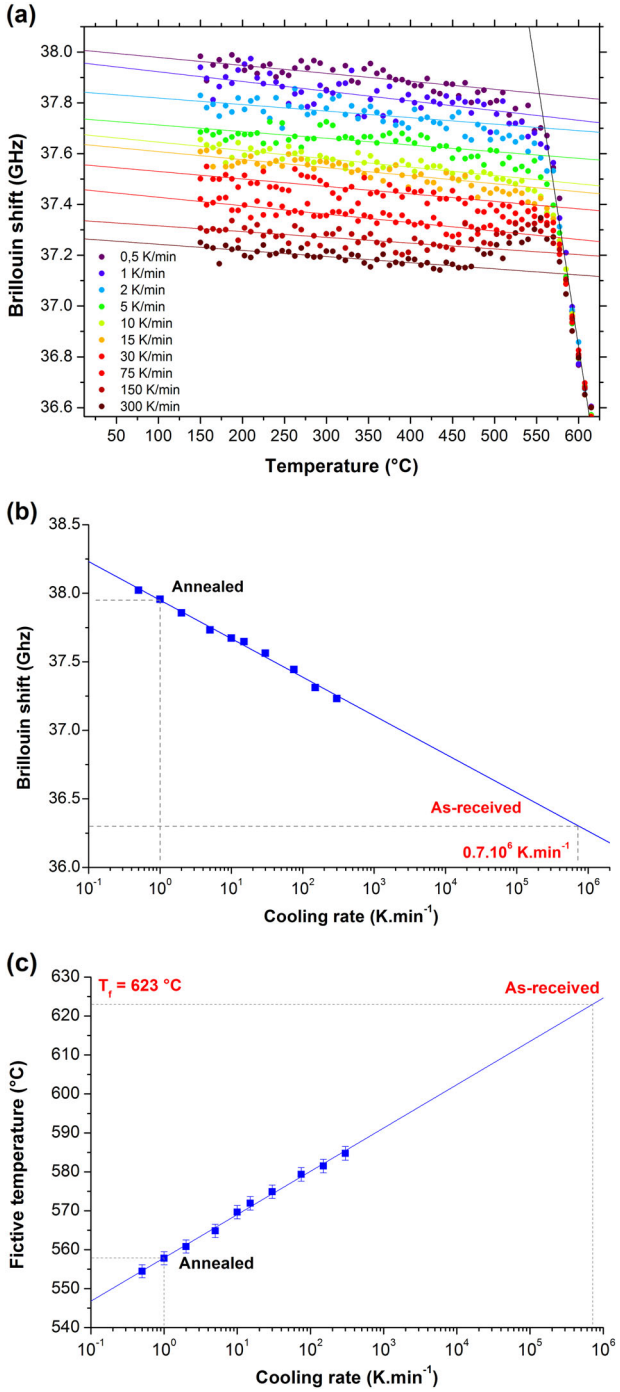


Fig. 1 **a** Brillouin shift as a function of temperature of ISG fibers cooled at different rates. **b** Brillouin shift extrapolated to room temperature as a function of the cooling rate of the fibers. The experimental error for confidence level of 95% was determined as ±0.08% of the mean value by realizing a map in an homogeneous sample (corresponding here to ±0.03 GHz which is the size of the square). The cooling rate predicted for the as-received fibers from its Brillouin shift is indicated in red. **c** Fictive temperature of ISG fibers as a function of the cooling rate. The fictive temperature error bars were estimated to be the deviation of the linear fits in **a**. The fictive temperature obtained for the as-received fibers from its cooling rate is indicated in red

thus offer a more free volume that facilitates interdiffusion. A recent work was performed on dissolution in pure water of annealed and melt-quenched binary and ternary borosilicate glasses.[17] It was found that glass compositions having the most significant structural variations after the thermal treatment, especially through boron coordinence, results in higher dissolution changes. We investigated here more complex glass composition through fibers, rapidly quenched during the drawing process and then annealed for reference (called in the paper "as-received fibers" and "annealed fibers", respectively). The International Simple Glass (ISG) was considered, a six-oxide reference glass widely used to examine the alteration in aqueous media of nuclear glasses.[18] Brillouin and Raman spectroscopies are respectively sensitive to acoustic (providing volume information) and optical (sensitive to local atomic vibrations) phonons. These techniques were used here to link glass structural and volume changes to cooling rates and the corresponding fictive temperatures. Structural changes between annealed and as-received fibers, and then between the pristine and altered fibers were characterized by multinuclear solid-state NMR spectroscopy, which is sensitive to both geometric and chemical disorder. Alteration experiments were performed at various stages of the reaction and different pHs. The forward dissolution rate, driven by hydrolysis mechanisms, was measured in media dilute enough to avoid any effect from the elements in solution on the alteration rate. The residual alteration rate, reflecting its long-term behavior, was obtained in initially silicon-saturated media (avoiding hydrolysis mechanisms[19]). Fibers ensured that the samples used in the dissolution experiments all had the same surface state, thus limiting surface-related uncertainties[20] in the measured rates.

RESULTS

Thermal history and thermodynamic properties of glass samples

Raman and Brillouin spectroscopies were used to evaluate the cooling temperature and fictive temperature of the glass fibers, in order to reveal their thermal history and quantify its effect. First of all, Brillouin and Raman calibration curves were measured in situ for bulk samples cooled at different rates. These data were then used to extract the quenching parameters of the as-received fibers. Differential scanning calorimetry (DSC) was used to address the thermodynamic properties of fibers.

Figure 1a shows the average position of the Brillouin shift for samples heated at 5 K min^{-1} between 150 and 620 °C after being subjected to various cooling rates between 0.5 K min^{-1} and 300 K min^{-1}. At the beginning of the heating process, the Brillouin shift is very sensitive to the initial cooling rate of the glass. This is consistent with the fact that the density and elastic properties of the glass decrease with the increase in quenching rate.[21,22] Between 150 and 450 °C, the Brillouin curves for the samples are all parallel, with a shallow slope. This evolution corresponds to thermal expansion, which is weakly sensitive to the initial cooling rate. Above the glass transition temperature ($T_g = 575$ °C), the Brillouin curves merge and decrease sharply, reflecting the complete relaxation of the glass structure. Some differences in behavior are observed between 450 °C and T_g. In the samples cooled more slowly, the glass structure remains into the equilibrated state during heating at 5 K min^{-1} and the transition to higher temperatures is smooth. For the samples cooled more rapidly on the other hand, at 75 K min^{-1} and above, heating at 5 K min^{-1} partially relaxes the glass before it becomes liquid like at higher temperatures.

Extrapolating the Brillouin curves to room temperature reveals the Brillouin shift corresponding to each of the quenching rates and yields the linear relationship shown in Fig. 1b. The Brillouin shift is greater, the slower the cooling rate is, in agreement with previous measurement on soda-lime glasses.[21] Extrapolating these

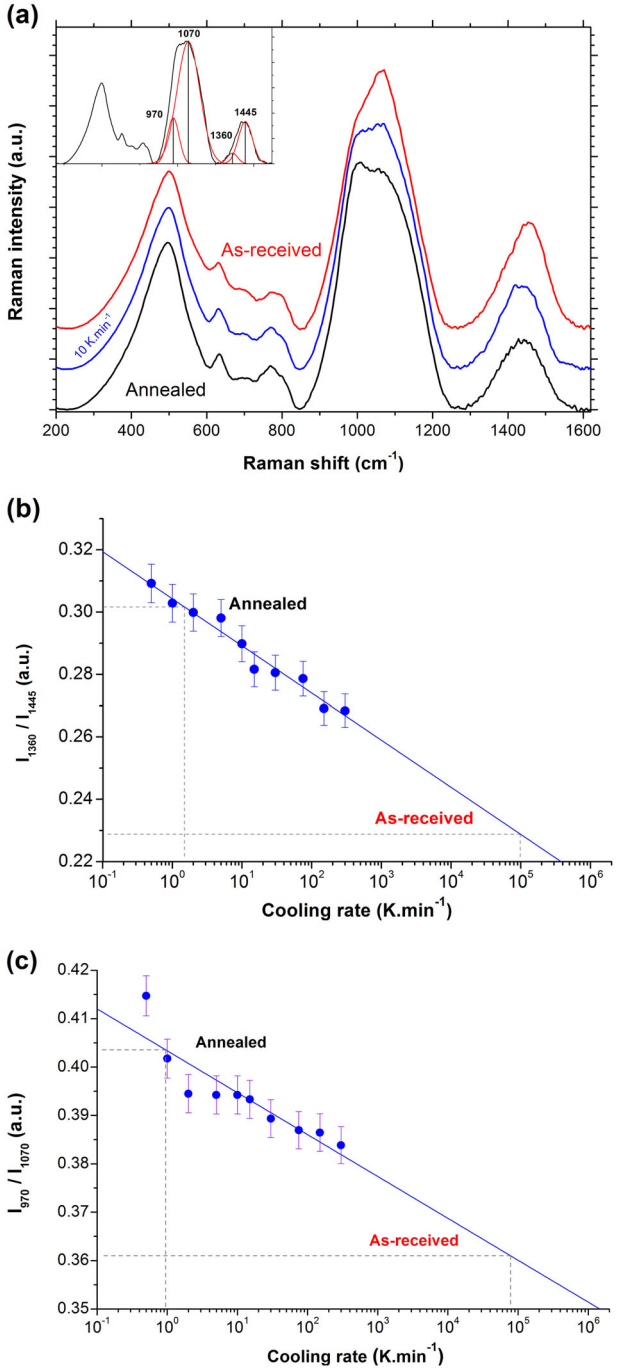


Fig. 2 **a** Raman spectra of the as-received and annealed ISG fibers, and of ISG cooled at 10 K min^{-1}. The inset shows the fit of the bands around 1000 cm^{-1} and 1400 cm^{-1}. **b**, **c** Intensity ratios as a function of cooling rate of the peaks (**b**) at 1360 cm^{-1} over the one at 1445 cm^{-1} and (**c**) at 970 cm^{-1} over the one at 1070 cm^{-1}. The error bars were taken as the standard deviation for the Gaussian fitting of the related peaks

shifts to the value measured for the as-received fibers (quenched during the drawing process) gives a quenching rate of 0.7×10^6 K min^{-1} (Fig. 1b). The intersections between the glass linear extrapolation and the liquid one in the Brillouin curves (Fig. 1a), which occur at the transition between the supercooled liquid and the frozen glass, give the Brillouin fictive temperature of the fibers. Figure 1c shows that the fictive temperature increases linearly with the cooling rate. The fictive temperature deduced for the as-received fibers (from the previous determined quenching rate of 0.7×10^6 K min^{-1}) is 623 °C. The same approach gives a fictive temperature for the annealed fibers of 558 °C, i.e., 65 °C lower.

Complementary glass local structural information can be obtained for specific structural groups by using the same method with Raman spectroscopy. We have shown previously on borosilicate glasses that the vibrations of SiO_4 and BO_3 groups are sensitive to variations of the glass fictive temperature.[7] Recent molecular dynamics simulations clearly highlighted these effects in ternary sodium borosilicate glasses in relation with the cooling rate.[23] Figure 2a compares the Raman spectra of as-received and annealed fibers and of the ISG bulk glass cooled at an intermediate rate (10 K min^{-1}). The inset shows contribution of the Gaussian components typically assigned to SiO_4 and BO_3 species whose variations were determined as a function of the cooling rate in Fig. 2b, c. The band around 1450 cm^{-1}, which consist of two Gaussian components, is assigned to stretching vibrations in BO_3 units.[24,25] We observed previously that the increase in intensity of this band was well correlated with the increase of the signal assigned to BO_3 units in ^{11}B MAS NMR spectra.[26] The narrow band around 630 cm^{-1}, assigned to vibrations from danburite-type B_2O_7–Si_2O_7 rings,[27] is slightly weaker in the spectrum of the as-received fibers. The ratio of the intensities of the peaks at 1360 cm^{-1} and 1445 cm^{-1} is plotted in Fig. 2b for cooling rates ranging from 0.5 to 300 K min^{-1}. By using least-square linear regression analysis, a cooling rate of about 10^5 K min^{-1} was obtained from the extrapolation of the data for the as-received fibers. The same approach was used for gaussian components at lower frequencies, in the large band between 830 cm^{-1} and 1275 cm^{-1} associated with the symmetric stretching modes in SiO_4 tetrahedra.[28,29] Plotting the ratio of the intensities of the peaks at 970 cm^{-1} and 1070 cm^{-1} as a function of the quenching rate yields a cooling rate for the as-received fibers of the same order as the one obtained from the boron vibrations (Fig. 2c). These values are about one order of magnitude lower than those calculated from the Brillouin data (close to 10^6 K min^{-1}). Another notable difference between these two datasets is that while the evolution of the Brillouin shift shows complex relaxation process between 450 °C and T_g, no equivalent perturbation was observed in the Raman data (peak intensity ratio vs temperature, Fig. 3).

Using the onset of the glass transition[30] for the sample cooled at 10 K min^{-1}, the glass transition temperature T_g was measured at 573 ± 1 °C. This value is in good agreement with previous works on ISG glass reporting 575 °C.[22] The difference in molar heat capacity near T_g, $\Delta C_P(T_g)$, between the annealed and as-received fibers was

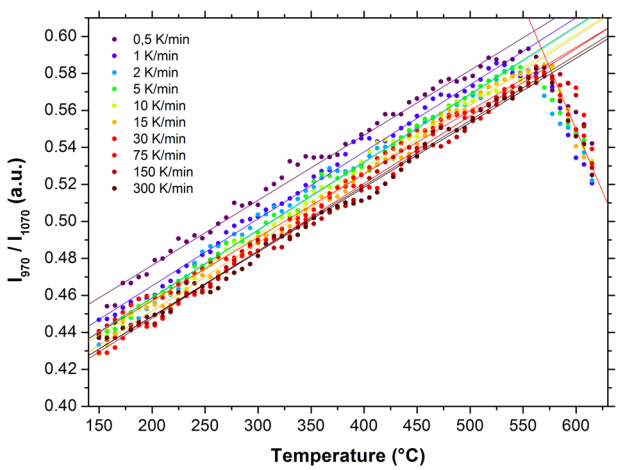


Fig. 3 Evolution of the intensity ratio of the fitted Raman band at 970 cm^{-1} over one at 1070 cm^{-1} as a function of temperature for ISG fibers cooled at different rates

measured to be 28.9 ± 0.3 J mol^{-1} K^{-1} which is comparable to the value of 28.1 ± 0.2 J mol^{-1} K^{-1} given in ref. [31] Using the respective Brillouin fictive temperature of the fibers (T_{f1} = 558 °C for the annealed ones and T_{f2} = 623 °C as-received) and assuming that the heat capacity does not vary much with the fictive temperature and that ΔC_P remains constant over the fictive temperature interval considered, this difference in heat capacity can be used to calculate the variations in thermodynamic properties. The difference of enthalpies of vitrification,

$$\Delta H_{v2} - \Delta H_{v1} = \int_{T_{f1}}^{T_{f2}} \left(C_{P_l}^{\circ} - C_{Pg}^{\circ}\right) dT \approx \Delta C_P(T_g) \times (T_{f2} - T_{f1}) \quad (1)$$

in which $C_{P_l}^{\circ}$ and C_{Pg}° are respectively the heat capacities of the liquid and the glass, is thus 1.88 kJ mol^{-1}. Likewise, the difference in configurational entropy, calculated using

$$S^{\circ}(0)_2 - S^{\circ}(0)_1 = \int_{T_{f1}}^{T_{f2}} \frac{C_{P_l}^{\circ} - C_{Pg}^{\circ}}{T} dT \approx \Delta C_P(T_g) \times \ln\left(\frac{T_{f2}}{T_{f1}}\right) \quad (2)$$

is found to be 2.18 J mol^{-1} K^{-1}. This gives a significant variation of Gibbs energy of formation,

$$\Delta G_f^{\circ}(298)_2 - \Delta G_f^{\circ}(298)_1 = (\Delta H_{v2} - \Delta H_{v1}) - 298\left(S^{\circ}(0)_2 - S^{\circ}(0)_1\right) \quad (3)$$

of 1.23 kJ mol^{-1} between the two samples.

Pristine glass structure

The NMR parameters for the different nuclei are listed in Table 1. As expected, the annealed fibers are slightly denser (about 1%) than the as-received fibers (Table 2).

Significant changes are observed between the ^{11}B MAS NMR spectra of the as-received and annealed fibers (Fig. 4a). The best fits obtained for the two spectra using methods described elsewhere,[26] put the proportion of tetrahedral boron in the annealed fibers at 50.0% vs 41.1% in the as-received ones (Fig. 5a, the fitting parameters are listed in Table 1). Rapid quenching is thus associated with a decrease of 8.9% in the proportion of BO_4 groups. The chemical shift of the BO_4 line is also more negative in the spectrum of the as-received fibers. This peak comes from boron atoms connected only to silicon atoms (^{4}B(4Si)) and from boron atoms connected to three silicon and one boron atoms (^{4}B(3Si,1B)).[26,32] Since the latter has more positive chemical shifts than the former, the observed shift in the BO_4 peak indicates that there is a larger proportion of ^{4}B(4Si) sites in the as-received fibers.

The ^{11}B MQMAS NMR spectra shown in Fig. 6a provide more accurate information on the distribution of boron sites in the fibers. The distributions of isotropic NMR shifts are broader in the as-received fibers than in the annealed ones, for both BO_3 and BO_4 groups, as highlighted by the projections onto the isotropic NMR shift axis (Fig. 6b).

Figure 4b shows that there is no significant change between the ^{29}Si MAS NMR spectra of the as-received and annealed fibers. This does not necessarily mean that the Q^n (n indicating the number of bridging oxygens per tetrahedron) speciation of the SiO_4 groups is identical in the two glasses. The ^{29}Si chemical shift of silicon groups is sensitive to the nature of their next-nearest neighbors. In previous works[7,33] we showed that the effects of depolymerization in the ^{29}Si NMR spectra were masked by an increased presence of boron as a next-nearest neighbor. It is generally expected that substitution of one bonded silicon for one aluminum impact the isotropic chemical shift of the central silicon by an increase of about 4–5 ppm.[34] Similar increase has been reported for Si–O–B linkages,[35,36] but shown to depend on the boron speciation[33] (no change is observed for Si–O–B^{III} in contrast to Si–O–B^{IV}). Because of the glass composition complexity, these data are therefore inconclusive as to possible differences in the degree of polymerization in the as-received and annealed fibers.

The single broad line in the ^{23}Na MAS NMR spectrum of the as-received fibers is slightly wider than the corresponding line for the annealed fibers (Fig. 7a). The interpretation of the width of ^{23}Na MAS NMR lines only, indicative of high substantial disorder, is tricky. ^{23}Na spin-echo experiments measuring ^{23}Na–^{23}Na dipolar couplings[37] were performed to investigate the spatial distribution of sodium. Indeed, the spin echo experiment refocuses most of the NMR interactions (giving the echo), except the homonuclear dipolar interactions which are only averaged out by MAS (to first order). Decay of the spin echo is therefore dominated by the effects of the ^{23}Na–^{23}Na dipolar interactions. Figure 7b shows that the ^{23}Na spin-echo signal from the as-received fibers decreases more rapidly, indicating that the ^{23}Na–^{23}Na dipolar couplings are much stronger than in the annealed fibers. This suggests that sodium is distributed less homogeneously in the as-received fibers.

The ^{27}Al MAS NMR line from the as-received fibers is broader than the one from the annealed ones (Fig. 7c), but no difference in the coordination of the aluminum atoms (tetrahedral in both cases, as confirmed by ^{27}Al MQMAS spectra given in Fig. 8) was observed. Differences in the chemical environment of aluminum atoms, particularly concerning their charge compensation, can be evaluated using the dipolar couplings between ^{23}Na and ^{27}Al nuclei, measured by heteronuclear rotational-echo double-resonance (REDOR) experiments.[38] The principle of REDOR, based on the spin echo experiment, is to collect two spin echo decay curves: the first denoted $S_0(t)$ using the standard pulse sequence 90°-τ-180°-τ; the second $S(t)$ applying on the second channel a train of rotor-synchronized refocusing 180° pulses (one at each rotor period and one in the middle of each rotor period), so that heteronuclear dipolar interactions are selectively reintroduced. The REDOR signal is obtained as $\Delta S(t) = (S_0(t) - S(t))/S_0(t)$ and only incorporates the effects of the dipolar heteronuclear interactions. Figure 7d clearly shows that the ^{23}Na{^{27}Al} REDOR signal from the as-received fibers is weaker, indicating that there are fewer aluminum atoms in the vicinity of sodium nuclei.

Table 1. Parameters used to fit the NMR spectra of ISG fibers

		As-received	Annealed
Na	δ_{iso} (ppm)	−11.1	−10.9
	C_Q (MHz)	2.2	2.2
	FWHM (ppm)	27.7	26.8
Al	δ_{iso} (ppm)	61.0	61.0
	C_Q (MHz)	5.2	4.7
	FWHM (ppm)	21.6	19.7
$BO_{4\ (3Si,1B)}$	δ_{iso} (ppm)	0.1	
	C_Q (MHz)	0.6	
	FWHM (ppm)	3.6	
	Population	30.6	42.1
$BO_{4\ (4Si,0B)}$	δ_{iso} (ppm)	−1.7	
	C_Q (MHz)	0.2	
	FWHM (ppm)	3.1	
	Population	10.5	7.9
$BO_{3\ ring}$	δ_{iso} (ppm)	17.2	
	C_Q (MHz)	2.5	
	Population	34.0	36.4
$BO_{3\ non-ring}$	δ_{iso} (ppm)	13.4	
	C_Q (MHz)	2.7	
	Population	24.9	13.6
$BO_{4\ total}$	Population	41.1	50.0

C_Q quadrupolar coupling constant, FWHM full width at half maximum

Table 2. Density and alteration rates for ISG fibers

Glass fibers		Forward dissolution rate ($g\,m^2\,d^{-1}$)			Mean residual rate ($g\,m^2\,d^{-1}$)	Equivalent thickness (nm)
	Density	$pH_{90\,°C}$ 6	$pH_{90\,°C}$ 7.5	$pH_{90\,°C}$ 9	pH 9	
Annealed	2.509	0.21	0.46	5.82	4.0×10^{-3}	444
As-received	2. 486	0.30	0.85	7.94	5.7×10^{-3}	957

Residual rates were calculated by linear regression between 72 and 224 days. The uncertainty associated with the rates is ±10%.

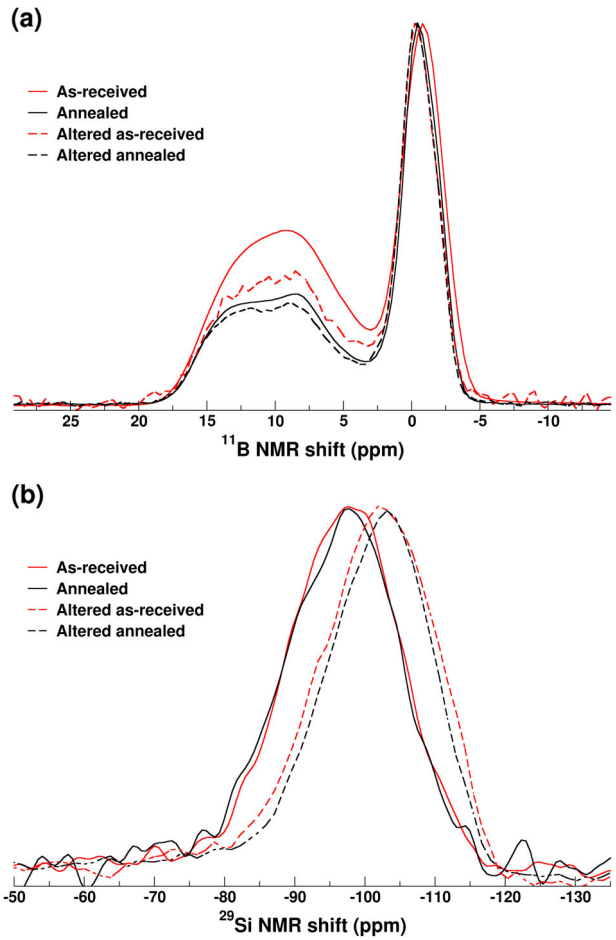


Fig. 4 **a** ^{11}B and **b** ^{29}Si MAS NMR spectra of as-received and annealed ISG fibers, either pristine (solid lines) or after 100 days of alteration at pH 7 and 90 °C (dashed lines). The spectra are scaled to the same height

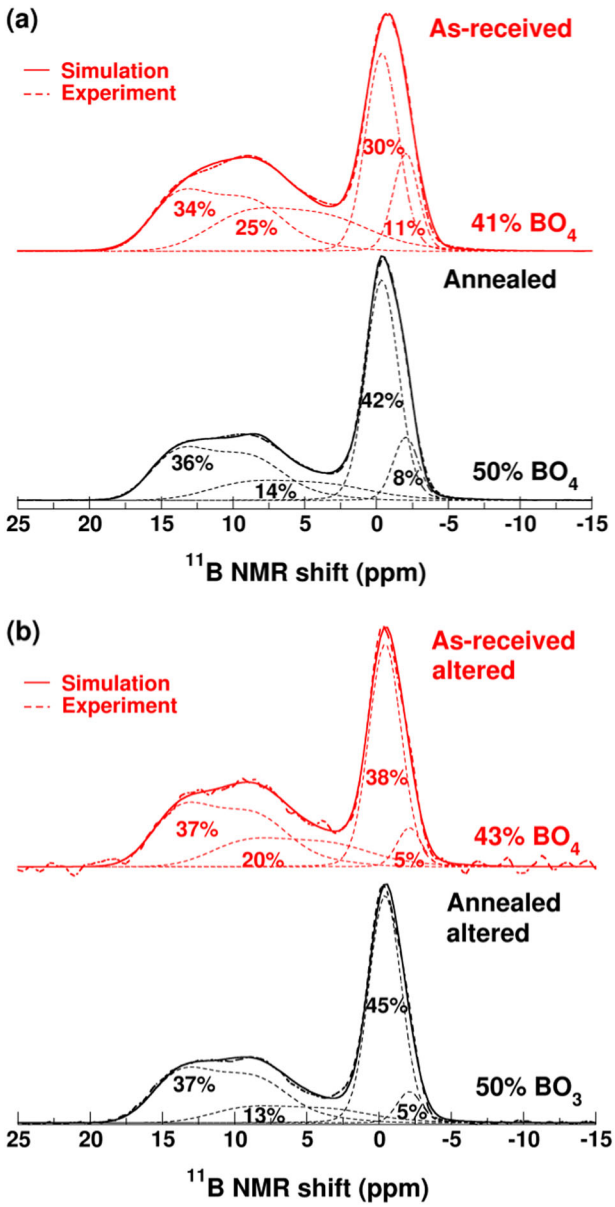


Fig. 5 Measured and simulated ^{11}B MAS NMR spectra of the as-received and annealed ISG **a** pristine fibers and **b** altered fibers, using the same peak positions and linewidths for all the spectra

Glass alteration far and close to saturation

Two types of experiments were performed on the as-received and annealed fibers to investigate their initial and long-term alteration behavior, namely when the alteration process in aqueous solutions is governed by hydrolysis of the silicate network, and after by the formation of a passivating layer.[19,39–41]

The first series of experiments were performed under forward dissolution rate conditions at 90 °C and pHs of 6, 7.5, and 9. The dissolution rates obtained from the measured silicon release rates are summarized in Table 2 and compared in Fig. 9a. Measurements of the aluminum concentration showed that the normalized mass losses were very close to that of silicon (data not shown). The pH dependence coefficient of the forward dissolution rates for both types of fibers is 0.4, in agreement to the value determined for SON68 glass.[42] The forward dissolution rates of the as-received fibers are higher under all three pH conditions than those of the annealed fibers, by a factor of 1.4–1.8.

Residual alteration rates were measured in solutions at pH 9 initially saturated with respect to amorphous silica, to investigate the effect of the alteration layer that forms on ISG fibers on its subsequent alteration.[19] No secondary phases precipitate on the

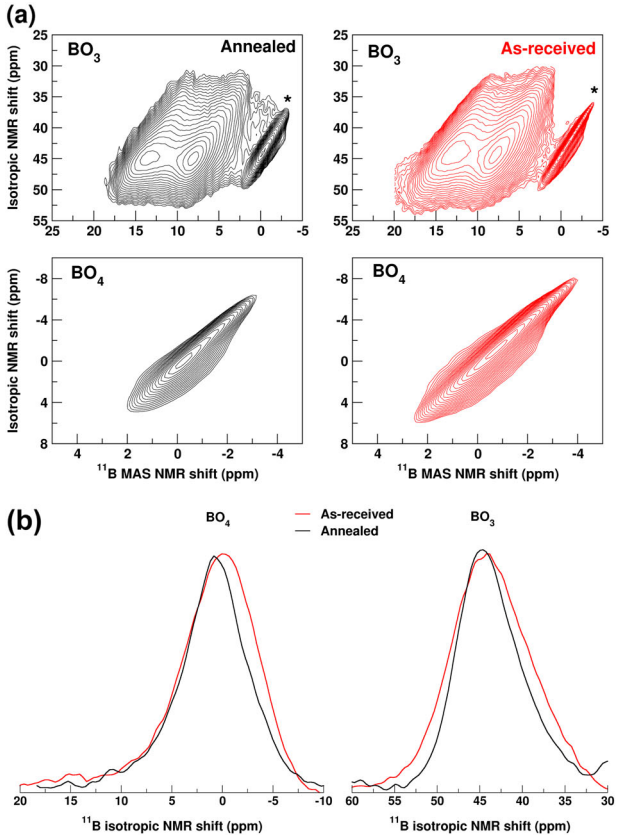


Fig. 6 **a** ^{11}B MQMAS NMR spectra of as-received and annealed ISG fibers (upper panels, BO_3 region; lower panels, BO_4 region) (*: spinning sidebands). **b** Projections onto the isotropic NMR shift axis of the spectra shown in part **a**

surface of ISG as it becomes altered, such that there is a direct link between the alteration rate of the glass and the passivating properties of the alteration layer.[6,43] The residual rate calculated according to the first data points (both from the Na and B release in solution) for the as-received fibers is about 2.4 times higher than the value obtained for the annealed fibers. This difference diminishes with time at about 1.4 considering the data points between 72 and 244 days (Table 2). Figure 9b shows the equivalent thicknesses of the altered layers at the end of the experiment that are about 2.2 times higher for as-received fibers. Analyses of the solutions indicate that the compositions of the alteration layers are almost identical (Table 3).

To investigate the structure of the alteration layer by NMR, a final experiment was performed under conditions chosen to maximize the proportion of the altered glass. Keeping constant the solution at pH 7 yielded a fraction of altered glass of 91% for the as-received fibers and 60% for the annealed fibers (calculated from solution analyses from boron release) after 100 days at 90 °C. This difference is consistent with the measurements performed at pH 9. As for the pristine samples, there is no observable change between the ^{29}Si MAS NMR spectra of the two types of fibers after alteration. Figure 4b shows however that the single broad peak observed in each case appears at a more negative chemical shift for the altered than the pristine glasses, highlighting the structural rearrangements occurring in the altered layer. The ^{29}Si chemical shift of silicate groups becomes more negative as the number of bridging oxygens increases (i.e., as the connectivity of the glass network increases); as shown above however, this variation could also be influenced by next-nearest neighbor effects. On the other hand, comparison of the ^{11}B MAS NMR spectra in Fig. 4a reveals that the proportion of trigonal boron is lower in the altered samples, mainly for the as-received fibers, indicating that BO_3 groups are released preferentially over BO_4 groups. Considering that 91% of the quenched fiber was altered and subtracting the pristine glass contribution, the resulting BO_3 proportion in the alteration layer is about 56.5% (58.9% in the as-received fibers). The proportion of boron species for altered fibers is given in Fig. 5b.

DISCUSSION

The Raman, Brillouin, and NMR spectroscopy data collected in this study provide complementary information on the structural changes induced by very rapid quenching of soda-lime aluminoborosilicate glass and the resulting effects on its chemical durability. Studying quenched samples reveals the effect of the thermal history, and thus of the fabrication process, on the properties of the glass. This approach can also be relevant to investigate the radiation damages in nuclear glasses, whose effects are similar to those of quenching.[8]

The Raman spectroscopy study might suggest that increasing the cooling rate should increase the average number of bridging oxygens per SiO_4 group since the peak contribution at 1070 cm^{-1}, usually assigned to high Q^n species, increases compared to the contribution at 970 cm^{-1}, usually assigned to lower Q^n species[44] (Fig. 2a). This observation is in agreement with in situ Raman data obtained on ISG glass with the increase of temperature.[22] An opposite trend was noted for sodium borosilicate glasses (without Zr and Al), whose degree of polymerization, as expected, was found to be lower the higher the fictive temperature was.[7,8] However, it is worth noting that the Si-O stretching region of the Q^n species is strongly affected by the presence of the T second-neighbors of Si (T = Zr, Al, B). Then, the decrease of the band at 970 cm^{-1} may be more likely related to the decrease of the Si atoms connected to two other second-neighbors than Si, Q^4(2T) units, overlapping the Q^2 units.[13] As we noticed for the boron with an increase of ^{4}B(4Si) instead of ^{4}B(3Si,1B) sites, quenched glasses could then limit mixing between network formers around Si atoms. The slight shift in the Si–O–Si bending mode from 496 cm^{-1} in the annealed sample to 500 cm^{-1} in the as-received fibers, suggests that the average Si–O–Si angle decreases with the increase of glass fictive temperature.[45] It has been reported that Si–O–Si bond angles tend to be smaller with the increase of Na in the vicinity of the Si groups,[46] which is in agreement here with the additional Na near Si in the as-received fibers coming from charge compensation of BO_4 groups in the annealed fibers.

The break in the overall trend observed in the Brillouin data between 450 °C and T_g for the glasses cooled most rapidly (Fig. 1a) was not observed in the Raman data (Fig. 3). This may be related to the lower relaxation energy of the groups probed by Raman spectroscopy which characterize the short-range order in the glass through iono-covalent bonds. At this length scale, the liquid to solid transition is similar at all quenching rates. The fact that the quenching rate determined from the Raman data for the as-received fibers (10^5 K min^{-1}) is close to a factor of ten lower than the value extrapolated from the Brillouin data (0.7×10^6 K min^{-1}) may also be due to the different length scales probed by the two techniques (short for the former and long for the latter). Fictive temperatures are traditionally determined by calorimetry, a bulk technique that is therefore presumably closer to the Brillouin than to the Raman data. The relatively good agreement between DSC and Brillouin is here confirmed by the fact that the Brillouin fictive temperature for a glass with a slow cooling rate of 10 K min^{-1} is of 570 ± 2 °C, within the error bar of the T_g at 573 ± 1 °C determined by DSC. Furthermore, the larger dispersion in the Raman measurements makes the extrapolations to determine the quenching rate of the as-received fibers more uncertain. The values obtained from the Brillouin data for the quenching rate

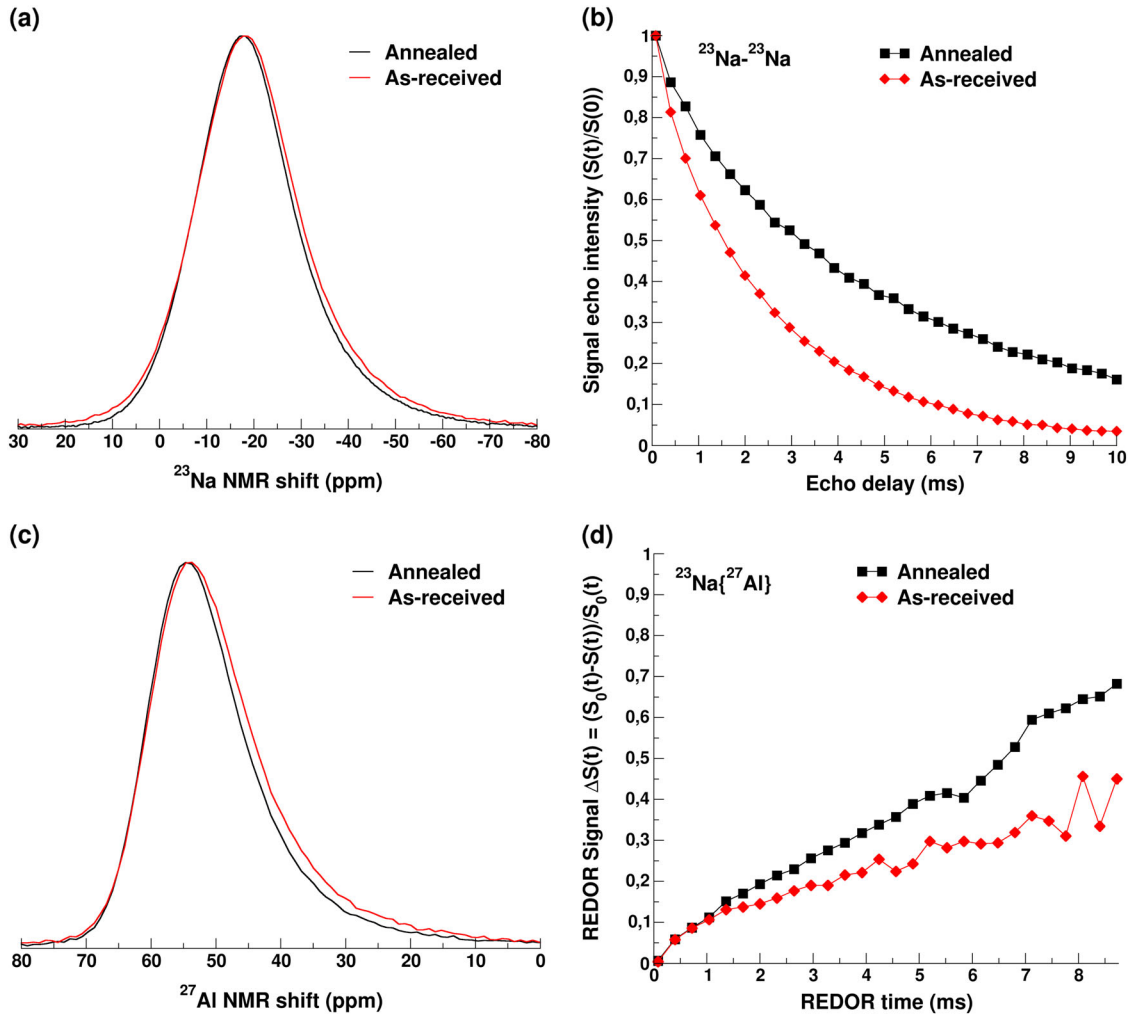


Fig. 7 **a** ^{23}Na MAS NMR spectra. **b** ^{23}Na spin-echo intensity as a function of the spin-echo delay. **c** ^{27}Al MAS NMR spectra, and **d** ^{23}Na{^{27}Al} rotational-echo double-resonance (REDOR) intensity as a function the REDOR time for as-received and annealed ISG fibers

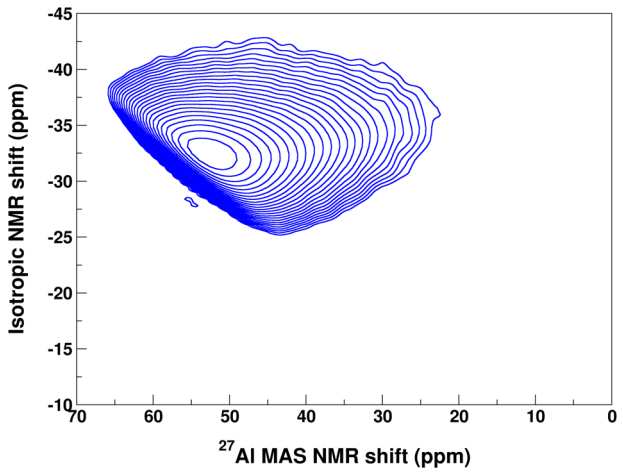


Fig. 8 ^{27}Al MQMAS NMR of the as-received ISG fibers

(0.7×10^6 K min^{-1}) and the fictive temperature (623 °C) therefore seem more reliable.

Multinuclear NMR first provides information on the structural disorder induced by rapid quenching. The ^{11}B MQMAS spectra (Fig. 6) show that the isotropic chemical shift distribution (δ_{iso}) is broader in the as-received fibers than once they are annealed. Since it was shown that ^{11}B δ_{iso} is sensitive to the B–O–(B, Si, or Al) bond angles in the glass,[33] these data suggest that the bond angle distribution of the as-received fibers is broader, thus reflective of an increased geometrical disorder. Regarding the cations in the glass, the ^{23}Na spin-echo experiments highlight that sodium is distributed more heterogeneously in the as-received fibers (the distance to the neighboring sodium atoms is shorter on average), possibly starting to form some alkaline clusters or local enrichment. In glasses with compositions similar to that of ISG, sodium acts mainly as a charge compensator, first for AlO_4 and then, for the residual Na available, for BO_4 groups.[47] The ^{23}Na–^{27}Al REDOR experiments clearly show that the proportion of sodium atoms in the vicinity of aluminum groups is lower in the as-received fibers. Since the coordination of aluminum does not change, part of aluminum groups must be charge compensated by other cations than sodium, here calcium. As a consequence, an increase of the quadrupolar splitting and thus the linewidth of the ^{27}Al MAS spectra is expected,[47,48] as actually observed here. Therefore, rather than compensate the charges of BO_4 and AlO_4 groups, part of the sodium ions in the as-received fibers acts as additional network modifiers, probably forming non-bridging oxygen bonds with silicon groups and adopting a less homogeneous distribution. Some of AlO_4 groups are Ca-compensated, while a part of BO_4 is transformed into BO_3 units.

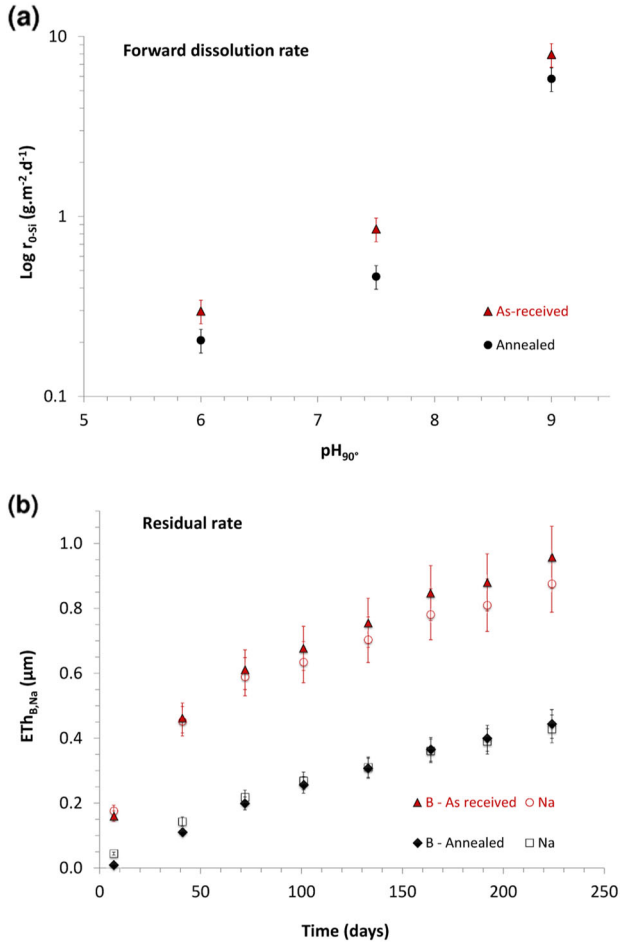


Fig. 9 **a** Forward dissolution rates as a function of pH (mean of measurements from triplicated experiments) and **b** equivalent thickness of the altered layer (measured from the normalized B and Na mass losses) as a function of leaching time at 90 °C for as-received and annealed ISG fibers. The uncertainty in the dissolution rates and equivalent thicknesses is 10%

Table 3. Chemical composition of altered layer deduced from solution analyses for ISG fibers altered for 224 days at 90 °C and pH 9

Altered layer (at%)	Si	Al	Ca	Zr
As-received	80.1	10.3	7.2	2.4
Annealed	80.3	10.4	6.9	2.4

The non-negligible difference in thermodynamic properties also reveals the effect of structural disorder. The variation of Gibbs energy of formation between as-received and annealed fibers (1.23 kJ mol^{-1}) is similar to the one between cristobalite and quartz (1.7 kJ mol^{-1}).[49] This difference, which is substantial with respect to the intrinsic stability of the glasses, suggests that their properties also differ. The difference of Gibbs energy could here be related to a variation of mean bond energy and an increase of disorder. As for SiO_2 polymorphs, the sample with the higher Gibbs energy will have a higher solubility.[50] It could also reflect the impact on the observed dissolution rates.

Leaching experiments clearly point out correlations between the thermally induced structural disorder of ISG and its chemical durability in solution at different stages of alteration. Under forward dissolution rate conditions at various pH near neutrality, between 6 and 9, the silicate network of the as-received fibers was hydrolyzed 1.4 to 1.8 times faster than that of the annealed fibers. Hydrolysis of the silicate glass network, which is the main mechanism governing the forward dissolution rate of the glass, is affected by the structural disorder. A higher NBO and BO_3 content and possibly a lower proportion of Si second-neighbors such as Zr or Al in the as-received fibers may also facilitate the hydrolysis reactions.[39,51,52] Same trends were noticed in a ternary sodium borosilicate glass with similar B_2O_3 content of about 18 mol%; a variation of T_f of 46 °C increased the BO_3 of 7.9%, resulting in a dissolution increase of about 1.5.[17] Glass compositions with higher boron concentration were subjected to lower boron coordinence variations between quenched and annealed samples. The difference was then also less pronounced concerning the dissolution behavior.[17]

The experiments performed under silicon saturation conditions show that the annealed glass dissolves faster than the quenched one. The difference between the two rates is maximal at the beginning of the experiment, which corresponds to the case of a more direct glass contact with the fluid since no passivating layer has yet formed. Because the composition of the onset solutions is the same, the difference of reactivity noticed at the beginning origins from structural differences between the two pristine glasses. Next, during alteration under silica saturated conditions, structural changes occurred within alteration layer. The AlO_4 et ZrO_6 groups mostly charge-balanced by sodium in the pristine glass become compensated by calcium in the altered layer, as has been reported previously for other silicate glasses[47] and more recently for ISG.[53] While as has been shown elsewhere,[19,43] boron is mostly absent from the altered layer, but trigonal boron groups are dissolved preferentially over tetrahedral units in the as-received fiber. Possible higher BO_3 grouping in the rapid quenched glass may enhance the release of mobile species in the residual rate regime. The faster residual alteration rate of the as-received fibers can also be explained by their more disordered structure (higher bond angle distribution, less-distributed alkalis and network formers around Si).

During aging of the alteration layer at higher reaction progress in the residual rate regime, the rate drops quickly because of the passivation layer growth.[19,43,54] Recent studies have shown that the alteration layer undergoes major reorganization owing to the high reactivity of the silicate network.[53–55] It results in the formation of a microporous, hydrated, amorphous material with a large majority of non-connected pores, strongly reducing water diffusion. Moreover, as the alteration layer is an evolving material undergoing pore ripening, due to incessant hydrolysis and condensation of siloxane bonds,[54] transport of aqueous species through the growing layer becomes rate-limiting. The present study points out that the residual rate of the two glasses becomes closer at longer duration. It can then be suggested that the passivating properties of the alteration layer, which are strongly linked to its reorganization,[39,56] will eventually dominate glass alteration after a first step of a control by the pristine glass structure. To confirm this interpretation, more research is needed to determine water dynamics in the alteration layers formed on the two glasses.

The structural differences between the as-received and annealed fibers can be compared directly with those induced by irradiation. The decrease of 8.9% in the proportion of BO_4 groups in the rapidly quenched glass is closer to the one observed in radioactive ISG doped with ^{244}Cm (7%),[12] than to the decrease induced in ISG by heavy-ions (Au) irradiation (13%).[13] Furthermore, whereas a change in aluminum coordination and depolymerization was observed for the irradiated glass,[12] no such changes were observed either for ^{244}Cm doped ISG[13] or for the quenched fibers in this study. These results therefore support the use of rapid quenching to mimic the effects of self-irradiation in nuclear glasses. This analogy could be used to study the

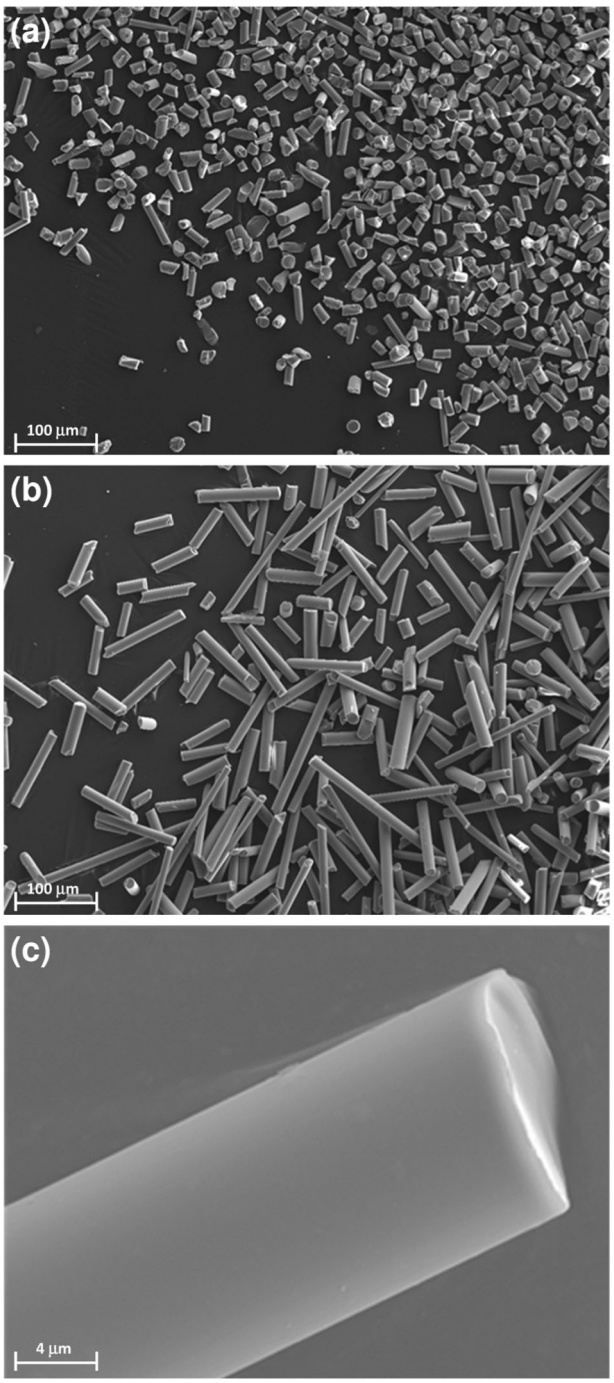


Fig. 10 Scanning electron micrographs of the chopped fibers, **a** 10–40 µm and **b** 63–250 µm in length. **c** Enlarged view of one of the fibers

mechanisms governing the chemical durability of high-activity nuclear glasses without having to handle radioactive samples.

METHODS

Sample preparation

The ISG glass ($60.1SiO_2$–$16.0B_2O_3$–$12.6Na_2O$–$3.8Al_2O_3$–$5.7CaO$–$1.7ZrO_2$) used in this study was prepared by MoSci Corporation (Rolla, MO, USA) and drawn into fibers having mean diameter of 12 µm by PPG industries, Inc. (Pittsburgh, PA, USA) (called "as-received fibers"). Some of the samples were annealed for 10 h at 575 °C to erase their thermal history and serve as a reference (called "annealed fibers").

For the alteration rate experiments, the fibers were cut into pieces either 10–40 µm or 63–250 µm in length (Fig. 10). Fine particles were then removed by successive washes in acetone and absolute ethanol by sedimentation. The particles in the 10–40 µm size had a geometric surface area of 1653 $cm^2\,g^{-1}$ but a surface area measured using the BET method of $3475 \pm 200\ cm^2\,g^{-1}$. This larger than expected surface area is due to the cutting process, which often left irregularities at the extremities of the cylinders. The geometric and BET surface areas are much closer for the larger particles, respectively 1384 $cm^2\,g^{-1}$ and $1440 \pm 80\ cm^2\,g^{-1}$. All the alteration rates were calculated from the BET values. Densities were measured by helium pycnometry (AccuPyc II1340, Micromeritics).

NMR

NMR data were collected on a Bruker Avance II 500WB spectrometer operating at a magnetic field of 11.72 T, using a Bruker 4 mm (outer diameter of the rotor) cross-polarization MAS XH probe at a spinning rate of 12.5 kHz. ^{11}B, ^{23}Na, and ^{27}Al MAS NMR spectra were acquired using short 1 µs pulses (corresponding to a tip angle of about $\pi/12$) to ensure a homogeneous excitation of all sites regardless of their quadrupolar coupling constant and thus obtain quantitative spectra. The recycle delays used were 1 s for the ^{23}Na and ^{27}Al and 2 s for the ^{11}B measurements. Typically, 1024 scans were accumulated. Two types of ^{11}B multiple-quantum MAS experiments were carried out in order to optimize the signal obtained from BO_3 and BO_4 units, as described previously.[26] ^{29}Si MAS NMR spectra were acquired using a saturation-recovery pulse sequence with a recovery delay of 20 s (increasing the recycling delay did not alter the lineshape). For spin-echo and REDOR experiments,[57,58] selective 90° and 180° pulses (frequency, 10–20 kHz; 180° pulse duration of 8–10 µs) were applied on the central transition (1/2↔1/2). The ^{23}Na–^{27}Al REDOR experiments were performed using a REDOR Box purchased from NMR Service GmbH, which splits the X-channel of the probe into a double-resonance circuit for close resonance frequencies (here $\nu_0^{Na} - \nu_0^{Al} \approx 2$ MHz).

The ^{11}B, ^{23}Na, ^{27}Al, and ^{29}Si NMR spectra were referenced externally respectively to 1 M aqueous boric acid (19.6 ppm relative to boron trifluoride etherate), 1 M aqueous NaCl (0 ppm), 1.0 M aqueous $Al(NO_3)_3$ (0 ppm), and tetrakis(trimethylsilyl)silane powder (two lines at −9.9 ppm and −35.3 ppm with respect to tetramethylsilane). A correction was applied for the ^{11}B MAS NMR spectra to account for the contribution of spinning sidebands to the BO_4 centerband, as described by Hopf et al.[51] The ^{11}B, ^{23}Na, and ^{27}Al MAS NMR spectra were fitted using NMR parameter distributions, as detailed elsewhere.[26,51,59] A single distribution was sufficient for the ^{23}Na and ^{27}Al spectra whereas at least four lines were required for the ^{11}B spectra, two for BO_3 units and two for BO_4 ones.

Raman, Brillouin spectroscopies, and DSC

Raman spectra were recorded using a Horiba iHR320 spectrometer with 1800 g mm^{-1} gratings, powered by a blue "Sapphire SF" 488 nm laser. Data were collected from 150 to 1700 cm^{-1}. The shorter laser wavelength is favorable for recording back scattered signals because of increased Rayleigh scattering, and allows data to be recorded at high temperatures without any overlap with black body radiation. The spectra were calibrated using a calcium carbonate reference. In order to compare spectra recorded at different temperatures, they were corrected for the wavelength and temperature Raman scattering dependence, described previously.[60] Brillouin spectra were recorded using a JRS TFP 2 HC tandem multi-pass Fabry–Perot interferometer. The different heat treatments were carried out in a PerkinElmer 8500 differential scanning calorimeter that was modified to allow in situ Raman and Brillouin measurements simultaneously. The approach used, dubbed ARABICA, has been described in detail by Veber et al.[61] Before each set of measurements the temperature was calibrated using α–β quartz and RbNO3 phase transitions which took place at 573 and 166 °C, respectively. All the measurements were carried out under a nitrogen gas flow of 30 mL min^{-1}

The calibration experiments were done using double side polished plane parallel plate of the ISG glass ($m = 28$ mg). The spectra were recorded during the heating up cycle after a period of cooling at a set rate. The cooling rates used were 300, 150, 75, 30, 15, 10, 5, 2, 1, and 0.5 K min^{-1}. For the in situ experiments the sample was placed in a platinum crucible covered with a pierced lid. The heating rate used was 5 K min^{-1} to leave enough time to properly collect Raman and Brillouin spectra. These were collected over the entire temperature range with an overall exposure time of 1.5 min (6 exposure cycles of 15 s each), such that a spectrum was recorded every 7.5 °C (1.5 min × 5 K min^{-1}). For the heat capacity

measurements a completely covered crucible was used. The heat flow measured by the calorimeter was calibrated using a sapphire disk.

Glass alteration experiments

All the alteration tests were performed at 90 ± 1 °C. The forward dissolution rate r_0 was measured in highly stirred static mode using perfluoroalkoxy reactors at a low surface area to volume (SA/V) ratio of about 5 m^{-1}. About 30 mg of glass fiber particles (63–250 µm in size) was placed in about 500 mL of solution. The forward dissolution rate (r_0) rate was measured in triplicate at $pH_{90°}$ 6 (adjusted with nitric acid), $pH_{90°}$ 7.5 (initially deionized water with a resistivity of 18.2 MΩ cm) and $pH_{90°}$ 9 (adjusted with lithium hydroxide). The solution was regularly sampled and the Si concentration was determined by colorimetry with a Merck Spectroquant kit and a Cary Varian UV–visible spectrophotometer. ICP-OES analyses were performed to check the release of other elements. The r_0 values were calculated from the normalized silicon mass loss, NL(Si), and correspond to the slope of NL(Si) as a function of time. The uncertainty in r_0 was estimated to be about 10%, taking into account errors in the measured surface area of the glass, in the silicon concentration, and the repeatability of the measurements.[20] The residual rates (r_r) were calculated from the normalized boron and sodium mass losses between 72 and 224 days. The associated uncertainty was also 10%. Variations in the surface area of the fibers were taken into account using a shrinking core model for cylinders.[62] The normalized mass losses, NL(*i*), (g m^{-2}) were calculated allowing for variations in the volume of the leaching solution (when samples were extracted) using the following equations:

$$\mathrm{NL}(i)_{n=1} = \frac{1}{x_i \cdot \mathrm{SA}} \cdot V_0 \cdot C_{j=1} \quad (4)$$

$$\mathrm{NL}(i)_{n>1} = \frac{1}{x_i \cdot \mathrm{SA}} \cdot \left[\left(V_0 - \sum_{j=1}^{j=n-1} V_j\right) \cdot C_{j=n} + \sum_{j=1}^{j=n-1} V_j \cdot C_j\right] \quad (5)$$

where C_j is the concentration of element i in the *j*th sample of the solution (g m^{-3}), x_i is the mass fraction of element *i* in the glass fiber, SA is the surface area (m^2) of the glass fibers in contact with the solution, V_0 is the initial volume (m^3) of the solution in the reactor, and V_j is the volume (m^3) of the *j*th sample.

Residual rate (r_r) measurements and the alteration experiments for NMR studies were carried out in non-stirred static mode using perfluoroalkoxy reactors. The altered glass studied by NMR was prepared by placing 300 mg of glass fiber particles (10–40 µm in size) in a silicon saturated solution ([Si] = 160 mg L^{-1}) at $pH_{90°}$ 7 ± 0.2. The SA/V ratio was 120 m^{-1} and the pH was kept constant throughout the experiment using nitric acid. For the residual rate measurements, 350 mg of glass fiber particles (10–40 µm in size) was altered at a SA/V ratio of 150 m^{-1} in a silicon saturated solution ([Si] = 260 mg L^{-1}) at $pH_{90°}$ 9 ± 0.1 (adjusted using lithium hydroxide). The pH of the solution remained constant throughout the experiment without any additional LiOH being required.

DATA AVAILABILITY

The data that support the findings of this study are available from the corresponding author upon reasonable request.

ACKNOWLEDGEMENTS

This work was supported by the French Alternative Energies and Atomic Energy Commission (CEA), ORANO and EDF.

AUTHOR CONTRIBUTIONS

F.A. and T.C. initiated the project. F.A. supervised the study and wrote the paper. T.C. performed the solid-state NMR study. P.J. performed the alteration experiments. D.d. L., M.B., and A.V. performed the Raman, Brillouin spectroscopies and DSC measurements. S.G. was involved in data interpretation. H.L. provided fibers from ISG glass. All the authors helped on paper writing and editing.

ADDITIONAL INFORMATION

Competing interests: The authors declare no competing interests.

Publisher's note: Springer Nature remains neutral with regard to jurisdictional claims in published maps and institutional affiliations.

REFERENCES

1. Devreux, F., Cailleteau, C. & Barboux, P. Evidence for a threshold in the biosolubility of aluminosilicate vitreous fibers. *J. Mater. Sci.* **45**, 1154–1159 (2010).
2. Kump, L. R., Brantley, S. L. & Arthur, M. A. Chemical, weathering, atmospheric CO2, and climate. *Annu. Rev. Earth Planet. Sci.* **28**, 611–667 (2000).
3. Angeli, F., Jollivet, P., Charpentier, T., Fournier, M. & Gin, S. Structure and chemical durability of lead crystal glass. *Environ. Sci. Technol.* **50**, 11549–11558 (2016).
4. Werme, L. et al. Chemical corrosion of highly radioactive borosilicate nuclear waste glass under simulated repository conditions. *J. Mater. Res.* **5**, 1130–1146 (1990).
5. Poinssot, C. & Gin, S. Long-term behavior science: the cornerstone approach for reliably assessing the long-term performance of nuclear waste. *J. Nucl. Mater.* **420**, 182–192 (2012).
6. Gin, S., Beaudoux, X., Angéli, F., Jégou, C. & Godon, N. Effect of composition on the short-term and long-term dissolution rates of ten borosilicate glasses of increasing complexity from 3 to 30 oxides. *J. Non-Cryst. Solids* **358**, 2559–2570 (2012).
7. Angeli, F. et al. Effect of temperature and thermal history on borosilicate glass structure. *Phys. Rev. B* **85**, 054110 (1-14) (2012).
8. Peuget, S. et al. Comparison of radiation and quenching rate effects on the structure of a sodium borosilicate glass. *J. Non-Cryst. Solids* **378**, 201–212 (2013).
9. Delaye, J. M., Peuget, S., Bureau, G. & Calas, G. Molecular dynamics simulation of radiation damage in glasses. *J. Non-Cryst. Solids* **357**, 2763–2768 (2011).
10. Maugeri, E. A. et al. Calorimetric study of glass structure modification induced by a decay. *J. Am. Ceram. Soc.* **95**, 2869–2875 (2012).
11. Peuget, S., Delaye, J. M. & Jegou, C. Specific outcomes of the research on the radiation stability of the French nuclear glass towards alpha decay accumulation. *J. Nucl. Mater.* **444**, 76–91 (2014).
12. Charpentier, T. et al. Self-healing capacity of nuclear glass observed by NMR spectroscopy. *Sci. Rep.* **6**, 6 (2016).
13. Mendoza, C. et al. Oxide glass structure evolution under swift heavy ion irradiation. *Nucl. Instrum. Methods Phys. Res. Sect. B-Beam Interact. Mater. At.* **325**, 54–65 (2014).
14. Mir, A. H. et al. Mono and sequential ion irradiation induced damage formation and damage recovery in oxide glasses: stopping power dependence of the mechanical properties. *J. Nucl. Mater.* **469**, 244–250 (2016).
15. Ya, M., Deubener, J. & Yue, Y. Z. Enthalpy and anisotropy relaxation of glass fibers. *J. Am. Ceram. Soc.* **91**, 745–752 (2008).
16. Amma, S., Luo, J. W., Kim, S. H. & Pantano, C. G. Effects of fictive temperature on the leaching of soda lime silica glass surfaces. *J. Am. Ceram. Soc.* **100**, 1424–1431 (2017).
17. Stone-Weiss, N. et al. Understanding the structural drivers governing glass-water interactions in borosilicate based model bioactive glasses. *Acta Biomater.* **65**, 436–449 (2018).
18. Gin, S. et al. An international initiative on long-term behavior of high-level nuclear waste glass. *Mater. Today* **16**, 243–248 (2013).
19. Gin, S. et al. Origin and consequences of silicate glass passivation by surface layers. *Nat. Commun.* **6**, 8 (2015).
20. Fournier, M. et al. Glass dissolution rate measurement and calculation revisited. *J. Nucl. Mater.* **476**, 140–154 (2016).
21. Levelut, C., Le Parc, R., Faivre, A. & Champagnon, B. Influence of thermal history on the structure and properties of silicate glasses. *J. Non-Cryst. Solids* **352**, 4495–4499 (2006).
22. Guerette, M. & Huang, L. P. In-situ Raman and Brillouin light scattering study of the international simple glass in response to temperature and pressure. *J. Non-Cryst. Solids* **411**, 101–105 (2015).
23. Deng, L. & Du, J. C. Effects of system size and cooling rate on the structure and properties of sodium borosilicate glasses from molecular dynamics simulations. *J. Chem. Phys.* **148**, 14 (2018).
24. Konijnendijk, W. L. & Stevels, J. M. Structure of borosilicate glasses studied by Raman-scattering. *J. Non-Cryst. Solids* **20**, 193–224 (1976).
25. Shibata, N., Horigudhi, M. & Edahiro, T. Raman-spectra of binary high-silica glasses and fibers containing GeO2 P2O5 and B2O3. *J. Non-Cryst. Solids* **45**, 115–126 (1981).
26. Angeli, F., Charpentier, T., de Ligny, D. & Cailleteauz, C. Boron speciation in soda-lime borosilicate glasses containing zirconium. *J. Am. Ceram. Soc.* **93**, 2693–2704 (2010).
27. Bunker, B. C., Tallant, D. R., Kirkpatrick, R. J. & Turner, G. L. Multinuclear nuclear-magnetic-resonance and Raman investigation of sodium borosilicate glass structures. *Phys. Chem. Glass.* **31**, 30–41 (1990).
28. Mysen, B. O., Finger, L. W., Virgo, D. & Seifert, F. A. Curve-fitting of Raman-spectra of silicate-glasses. *Am. Miner.* **67**, 686–695 (1982).
29. McMillan, P. Structuralstudies of silicate-glasses and melts - applications and limitations of raman-spectroscopy. *Am. Miner.* **69**, 622–644 (1984).

30. Yue, Y. Z. Characteristic temperatures of enthalpy relaxation in glass. *J. Non-Cryst. Solids* **354**, 1112–1118 (2008).
31. Linard, Y., Yamashita, I., Atake, T., Rogez, J. & Richet, P. Thermochemistry of nuclear waste glasses: an experimental determination. *J. Non-Cryst. Solids* **286**, 200–209 (2001).
32. Angeli, F. et al. Influence of lanthanum on borosilicate glass structure: a multinuclear MAS and MQMAS NMR investigation. *J. Non-Cryst. Solids* **376**, 189–198 (2013).
33. Soleilhavoup, A., Delaye, J. M., Angeli, F., Caurant, D. & Charpentier, T. Contribution of first-principles calculations to multinuclear NMR analysis of borosilicate glasses. *Magn. Reson. Chem.* **48**, S159–S170 (2010).
34. Florian, P., Veron, E., Green, T. F. G., Yates, J. R. & Massiot, D. Elucidation of the Al/Si ordering in gehlenite Ca2Al2SiO7 by combined Si-29 and Al-27 NMR spectroscopy/quantum chemical calculations. *Chem. Mater.* **24**, 4068–4079 (2012).
35. Nanba, T., Asano, Y., Benino, Y., Sakida, S. & Miura, Y. Molecular orbital calculation of the Si-29 NMR chemical shift in borosilicates: the effect of boron coordination to SiO4 units. *Phys. Chem. Glass.-Eur. J. Glass Sci. Technol. Part B* **50**, 301–304 (2009).
36. Nanba, T., Nishimura, M. & Miura, Y. A theoretical interpretation of the chemical shift of Si-29 NMR peaks in alkali borosilicate glasses. *Geochim. Cosmochim. Acta* **68**, 5103–5111 (2004).
37. Ratai, E., Janssen, M. & Eckert, H. Spatial distributions and chemical environments of cations in single- and mixed alkali borate glasses: evidence from solid state NMR. *Solid State Ion.* **105**, 25–37 (1998).
38. Gullion, T. & Schaefer, J. Rotational-echo double-resonance NMR. *J. Magn. Reson.* **81**, 196–200 (1989).
39. Cailleteau, C. et al. Insight into silicate-glass corrosion mechanisms. *Nat. Mater.* **7**, 978–983 (2008).
40. Vienna, J. D., Ryan, J. V., Gin, S. & Inagaki, Y. Current understanding and remaining challenges in modeling long-term degradation of borosilicate nuclear waste glasses. *Int. J. Appl. Glass Sci.* **4**, 283–294 (2013).
41. Frugier, P. et al. SON68 nuclear glass dissolution kinetics: current state of knowledge and basis of the new GRAAL model. *J. Nucl. Mater.* **380**, 8–21 (2008).
42. Advocat, T., Crovisier, J. L., Vernaz, E., Ehret, G. & Charpentier, H. *Hydrolysis of R7t7 Nuclear Waste Glass In Dilute Media - Mechanisms and Rate as a Function of pH*. Vol. 212 (Materials Research Soc., Boston, 1991).
43. Gin, S. et al. Atom-probe tomography, TEM and ToF-SIMS study of borosilicate glass alteration rim: a multiscale approach to investigating rate-limiting mechanisms. *Geochim. Cosmochim. Acta* **202**, 57–76 (2017).
44. Neuville, D. R., de Ligny, D. & Henderson, G. S. in *Spectroscopic Methods in Mineralology and Materials Sciences*, Vol. 78 (eds G. S. Henderson, D. R. Neuville & R. T. Downs) 509–541 (Mineralogical Society of America, Chantilly, 2014).
45. Matson, D. W., Sharma, S. K. & Philpotts, J. A. The structure of high-silica alkali-silicate glasses. A Raman spectroscopic investigation. *J. Non-Cryst. Solids* **58**, 323–352 (1983).
46. Angeli, F., Villain, O., Schuller, S., Ispas, S. & Charpentier, T. Insight into sodium silicate glass structural organization by multinuclear NMR combined with first-principles calculations. *Geochim. Cosmochim. Acta* **75**, 2453–2469 (2011).
47. Angeli, F., Gaillard, M., Jollivet, P. & Charpentier, T. Influence of glass composition and alteration solution on leached silicate glass structure: a solid-state NMR investigation. *Geochim. Cosmochim. Acta* **70**, 2577–2590 (2006).
48. Angeli, F., Gaillard, M., Jollivet, P. & Charpentier, T. Contribution of Ca-43 MAS NMR for probing the structural configuration of calcium in glass. *Chem. Phys. Lett.* **440**, 324–328 (2007).
49. Robie, R. A. & Hemingway, B. S. *Thermodynamic Properties of Minerals and Related Substances at 298.15 K and 1 Bar (105 Pa) Pressures and at Higher Temperatures*., Vol. 2131 (US Geological Survey Bulletin, Washington, 1995).
50. Fournier, R. O. & Rowe, J. J. Solubility of cristobalite along 3-phase curve, gas plus liquid plus cristobalite. *Am. Miner.* **47**, 897–89 (1962).
51. Hopf, J. et al. Glass-water interaction: effect of high-valence cations on glass structure and chemical durability. *Geochim. Cosmochim. Acta* **181**, 54–71 (2016).
52. Bergeron, B. et al. First investigations of the influence of IVB elements (Ti, Zr, and Hf) on the chemical durability of soda-lime borosilicate glasses. *J. Non-Cryst. Solids* **356**, 2315–2322 (2010).
53. Collin, M. et al. Structure of international simple glass and properties of passivating layer formed in circumneutral pH conditions. *npj Mater. Degrad.* **2**, 4 (2018).
54. Gin, S. et al. Dynamics of self-reorganization explains passivation of silicate glasses. *Nat. Commun.* **9**, 2169 (2018).
55. Collin, M., Fournier, M., Charpentier, T., Moskura, M. & Gin, S. Impact of alkali on the passivation of silicate glass. *npj Mater. Degrad.* **2**, 16 (2018).
56. Cailleteau, C., Devreux, F., Spalla, O., Angeli, F. & Gin, S. Why do certain glasses with a high dissolution rate undergo a low degree of corrosion? *J. Phys. Chem. C* **115**, 5846–5855 (2011).
57. Bertmer, M., Zuchner, L., Chan, J. C. C. & Eckert, H. Short and medium range order in sodium aluminoborate glasses. 2. Site connectivities and cation distributions studied by rotational echo double resonance NMR spectroscopy. *J. Phys. Chem. B* **104**, 6541–6553 (2000).
58. Janssen, M. & Eckert, H. B-11{Na-23} rotational echo double resonance NMR: a new approach for studying the spatial cation distribution in sodium borate glasses. *Solid State Ion.* **136**, 1007–1014 (2000).
59. Quintas, A. et al. NMR study of a rare-earth aluminoborosilicate glass with varying CaO-to-Na2O ratio. *Appl. Magn. Reson.* **32**, 613–634 (2007).
60. McMillan, P. F., Poe, B. T., Gillet, P. & Reynard, B. A study of SiO2 glass and supercooled liquid to 1950 K via high-temperature raman-spectroscopy. *Geochim. Cosmochim. Acta* **58**, 3653–3664 (1994).
61. Veber, A., Cicconi, M. R., Reinfelder, H. & de Ligny, D. Combined differential scanning calorimetry, Raman and Brillouin spectroscopies: a multiscale approach for materials investigation. *Anal. Chim. Acta* **998**, 37–44 (2018).
62. Gin, S., Frugier, P., Jollivet, P., Bruguier, F. & Curti, E. New insight into the residual rate of borosilicate glasses: effect of S/V and glass composition. *Int. J. Appl. Glass Sci.* **4**, 371–382 (2013).

Open Access This article is licensed under a Creative Commons Attribution 4.0 International License, which permits use, sharing, adaptation, distribution and reproduction in any medium or format, as long as you give appropriate credit to the original author(s) and the source, provide a link to the Creative Commons license, and indicate if changes were made. The images or other third party material in this article are included in the article's Creative Commons license, unless indicated otherwise in a credit line to the material. If material is not included in the article's Creative Commons license and your intended use is not permitted by statutory regulation or exceeds the permitted use, you will need to obtain permission directly from the copyright holder. To view a copy of this license, visit http://creativecommons.org/licenses/by/4.0/.

© The Author(s) 2018